

Integrable Floquet Time Crystals in One Dimension

Rahul Chandra¹, Mahbub Rahaman², Soumyabroto Majumder¹, Anlabha Roy^{1,*} and Sujit Sarkar³

¹Department of Physics, The University of Burdwan, Bardhaman, West Bengal 713104, India

²Harish-Chandra Research Institute, A CI of Homi Bhabha National Institute, Prayagraj, Uttar Pradesh 211019, India

³Theoretical Sciences Department, Poornaprajna Institute of Scientific Research, Bangalore 562164, India

(Dated: April 21, 2026)

We demonstrate the realization of a Discrete Time-Crystal (DTC) phase in a family of periodically driven, one-dimensional quadratic lattice Hamiltonians that can be obtained using spin chains. These interactions preserve integrability while opening controllable gaps at resonant quasienergies and pinning the emergent quasienergy modes that are responsible for subharmonics. We demonstrate that the DTC phase is rigid in the parameter space of transverse field and an additional interaction like Next-Nearest-Neighbor (NNN) coupling strength, with the drive frequency optimized to produce the strongest subharmonic response. We also provide a detailed phase diagram of the model, exhibiting a Floquet Paramagnet (FPM) phase, as well as sharp quantum phase transitions between the FPM and the DTC. Finite-size scaling of the Floquet quasienergy splitting between the emergent subharmonic mode and its conjugate shows that the DTC lifetime diverges exponentially with system size. Thus, our work establishes a novel mechanism for achieving robust long-lived DTCs in one dimension. Motivation for this work stems from the limitations of disorder-based stabilization schemes that rely on many-body localization and exhibit only prethermal or finite-lived plateaus, eventually restoring ergodicity. Disorder-free routes are therefore highly desirable. Integrable (or Floquet-integrable) systems provide an attractive alternative because their extensive set of conserved quantities and constrained scattering strongly restrict thermalization channels. Our construction exploits these integrable restrictions together with longer-range NNN engineering to produce a clean, robust DTC that avoids the prethermal fragility of disordered realizations.

Keywords: Discrete Time-Crystal, Floquet Time Crystal, Integrable Systems, Spin Chains, Quantum Phase Transitions

I. INTRODUCTION

Spontaneous symmetry breaking (SSB) is the key principle that governs emergent order in many-body systems. Following Wilczek's proposal of time-crystals [1, 2], which envisioned phases breaking the continuous-time translation symmetry in equilibrium, a sequence of no-go theorems established that such equilibrium-time crystals cannot arise in generic short-range Hamiltonians [3, 4], steering interest toward intrinsically non-equilibrium settings. In periodically driven (Floquet) systems, for instance, the *Discrete* time-translation symmetry may break spontaneously, producing Discrete Time-Crystals (DTC) with robust subharmonic response, spatiotemporal long-range order, and rigidity to perturbations [5]. These criteria, now standard in the community, underlie both theory [6, 7] and experiment [8, 9] and provide the baseline against which we position our results.

The central challenge underlying stable subharmonic (period-doubled) response in Discrete Time-Crystals is preventing melting of the subharmonic plateau under generic perturbations and finite-size or finite-time effects [10–12]. Early realizations of driven Ising-like chains employed disorder-induced many-body localization (MBL) [9, 13, 14] to inhibit heating between nominal π -pulses in spin-echo-style Floquet sequences [5, 15, 16], thus stabilizing emergent $2T$ oscillations. However, such disorder-stabilized DTCs typically enter a prethermal regime [10, 17, 18] with an extended but ultimately finite-lived subharmonic plateau that decays once residual interactions or processes in rare regions restore ergodicity [19, 20]. (See, e.g., prethermal plateau analyses and

lifetime scaling discussions in works associated with Huse and collaborators. [13, 21–24])

These limitations motivate the search for disorder-free, clean, and symmetry-protected routes to persistent subharmonics [25–27]. Continuous (as opposed to discrete) time crystal behavior in driven or pumped Bose–Einstein condensates (e.g. Keßler, Hemmerich and related cavity/BEC platforms) [28–33] exemplifies an alternative mechanism. Other proposals involve quantum many-body scars [34–37], dynamical many-body localization [38], flat-bands [39] and strong Stark potentials [12, 40]. In parallel, a distinct disorder-free pathway [41, 42] emerges in integrable or Floquet-integrable systems [41, 43, 44]: exact (or quasi-exact) conservation laws [45, 46], strong (or almost strong) π modes [47, 48], and constrained quasiparticle scattering [49, 50] combine to pin subharmonic responses without the need for localization [15, 51, 52]. Recent work [44, 48, 53] shows that one-dimensional integrable systems can be realized in quantum simulators [54–58], and quantum dynamics can be engineered by Trotterization [59, 60].

Earlier demonstrations of disorder-free time-crystalline behavior in integrable models include the driven Lipkin–Meshkov–Glick (LMG) system [61], in which period-doubling originates from symmetry-broken collective states and associated quasi-energy doublets; periodically driven BCS condensates that exhibit parametric resonances [62] and realize commensurate time-crystal phases within Arnold tongues; and p -spin models with infinite-range interactions that support higher-order subharmonic responses [63]. These realizations, however, are subject to important limitations. In the driven LMG model, the periodic drive destroys integrability [64], while the other setups rely on semiclassical limits. In contrast, the present work investigates the exact quantum dynamics of a

* Corresponding author: Email daneel@utexas.edu

fully integrable one-dimensional lattice model, wherein time-crystalline behavior arises from momentum-resolved quasiparticle dynamics and Floquet band engineering enabled by next-nearest-neighbour couplings.

Our earlier work [65] demonstrated the onset of Discrete Time-Crystalline order in higher-dimensional integrable lattices, but revealed a fragility upon dimensional reduction to strictly one dimension. The key bottleneck was an insufficient parameter manifold to simultaneously (i) satisfy resonant mode pinning conditions, (ii) open and control quasienergy gaps at the relevant π (or near- π) quasienergies, and (iii) suppress dephasing channels associated with nearby continua in momentum space. In the present work, we remedy that dimensional fragility by introducing controlled next-nearest-neighbor (NNN) (and effectively longer-range multi-spin) couplings that (a) preserve integrability, (b) enlarge the tunable parameter space, and (c) generate adjustable Bogoliubov (and Floquet) gap structures that robustly isolate a subharmonic mode. This converts a previously fragile (fine-tuned) subharmonic into a rigid phase protected by symmetry and sustained over an extended region in the parameter space.

Conceptually, the approach illustrates that NNN extensions, rather than truly long-range algebraic tails, suffice for stabilization in a clean, translationally invariant setting. The added NNN (or three-spin Jordan–Wigner–generated) structures supply just enough dispersion engineering to ensure (i) controllable quasienergy gap opening at resonance, (ii) momentum-selective mode pinning (a π -mode analog) and (iii) suppression of multimode dephasing by reducing accidental degeneracies. Thus, integrability is leveraged not only as an analytical simplifier but also as an active stabilizing mechanism for Floquet subharmonics, offering a disorder-free counterpart to MBL- or prethermality-based stabilization routes. We therefore position this work at the intersection of: (1) the ongoing program of disorder-free or clean DTC realization, (2) the exploitation of strong / almost strong mode physics in integrable and Floquet-integrable spin and fermionic chains, and (3) dimensional reduction strategies that retain controllable resilience of subharmonic order without invoking long-range interactions or open-system engineering. The resulting phase diagram, which contains robust DTC and Floquet Paramagnet (FPM) regimes, provides a unified framework for testing how integrability shapes temporal symmetry breaking, quasienergy topology, and finite-size scaling of melting times.

Concretely, in this manuscript we map the Floquet phase diagram in a manifold of Hamiltonian parameters consisting of the periodic drive amplitude g_0 and, for concreteness, an NNN coupling strength λ added to the Ising spin chain. We optimize the drive frequency to maximize the stability of the DTC phase and identify a contiguous DTC region bounded by analytically obtained Floquet gapless points at both high-symmetry and non-high-symmetry momenta; adjacent to these boundaries we find FPM behavior. Thus, a rich phase diagram emerges with sharp quantum transitions involving DTC in an exact, integrable, closed quantum system that goes beyond the simple symmetry-broken/thermal phase transitions seen in MBL systems[6], and in analogy with recently studied phase transitions in fractal time crystals in the mean-field limit[66],

as well as open quantum systems[67].

Dynamically, the DTC is diagnosed by near-unity long-time-averaged fidelity at optimal momentum k_0 and a robust stroboscopic correlation $\overline{C_z} \sim \mathcal{O}(1)$, while the FPM shows suppressed fidelity and qualitatively different temporal signatures. Further analysis of these phases involves scaling hypothesis tests on temporal long-range correlations, which demonstrate the onset of off-diagonal long-range order (ODLRO) in time for the DTC phase and rapid decay of these correlations near criticality in the FPM phase, justifying the nomenclature chosen. Finally, we extract a splitting $\delta\Omega(N)$ of the subharmonic peak from finite-size analyzes of the stroboscopic signal (FFT of $C_z(k_0^R, nT)$), and fit scaling laws $\delta\Omega \sim N^\alpha$: deep in the DTC we obtain algebraic scaling with $\alpha \approx -1$ (beat period $\sim N$), while in FPM the splitting either broadens, plateaus, or yields unstable exponents. These scaling results are obtained robustly through two Lorentzian peak fits and regression by Random Sampled Consensus (RANSAC). RANSAC is a robust algorithm used in machine learning [68, 69] that suppresses outliers from failed double-peak fits or resolution-limited spectra. Successful hypothesis tests have provided very clear finite-size distinctions between the truly rigid DTC order and FPM behavior.

Beyond establishing stability, our analysis clarifies how integrability is responsible for the rigidity of the DTC phase. In particular, we connect subharmonic oscillations to (a) the structure of conserved charges in the quadratic fermion description, (b) π -mode pinning akin to strong-mode physics in Floquet-integrable chains and circuits, and (c) finite-size dependence of melting of the DTC at accessible drive frequencies that complement, rather than substitute for, exact integrable control. This synthesis allows for the realization of DTCs by methods previously developed for one-dimensional integrable chains and circuits, providing a unified route to subharmonic order in clean systems.

Thus, our results should be read alongside three intertwined lines of inquiry.

1. Clean DTCs without disorder: high-frequency prethermal DTCs in generic systems and domain-wall-confined DTCs in kicked chains supply complementary stabilization routes; our models realize rigidity without relying on either MBL or all-to-all interactions.
2. Integrable / Floquet-integrable diagnostics: Strong and almost strong mode analyses in Floquet spin chains and integrable XXZ circuits motivate our π -mode pinning picture and guide our spectral tests.
3. Higher-dimensional integrable free fermions: [65] established the feasibility of higher-D integrable DTCs; we extend that framework by showing that NNN couplings within the integrable class enhance stability and broaden parameter windows for subharmonic order.

Our work is organized as follows. In Section II, we introduce the basic model and its dynamics. In Section III, we present analytical and numerical explorations of the dynamics of the order parameter, building a complete phase profile of the system, and demonstrating quantum phase transitions between

the DTC and FPM phases. We also elucidate how integrability ensures rigidity of the DTC phase in a three-parameter space of drive frequency, transverse field, and NNN coupling strength. In Section IV, we present the finite-size scaling of stroboscopic correlations, compared against exact numerics. Finally, we present our conclusions and outlook.

II. THE BASIC MODEL AND DYNAMICS

Consider the class of spinless free-fermionic models represented by a quadratic Bogoliubov-de Gennes (BdG) Hamiltonian summed over momentum pairs in the First Brillouin Zone (FBZ) of a one-dimensional lattice:

$$H = \sum_{k,-k} \hat{\Psi}_k^\dagger H_k(t) \hat{\Psi}_k \quad (1)$$

where, $\hat{\Psi}_k^\dagger = \begin{pmatrix} c_k^\dagger & c_{-k} \end{pmatrix}$ is a Nambu spinor and c_k^\dagger (c_k) are fermionic creation (annihilation) operators. The BdG Hamiltonian $H_k(t)$ consists of a time-dependent 2×2 traceless Hermitian matrix given by $\mathbf{r}_k(t) \cdot \boldsymbol{\tau}$, where the vector of Pauli matrices $\boldsymbol{\tau} = \tau_1 \hat{x} + \tau_2 \hat{y} + \tau_3 \hat{z}$ consists of three matrices $\tau_{1,2,3}$ given by $\tau_1 = \begin{pmatrix} 0 & 1 \\ 1 & 0 \end{pmatrix}$, $\tau_2 = \begin{pmatrix} 0 & -i \\ i & 0 \end{pmatrix}$, $\tau_3 = \begin{pmatrix} 1 & 0 \\ 0 & -1 \end{pmatrix}$, and the Bloch vector $\mathbf{r}_k(t) \sim \Xi_k(t) \hat{x} + \Upsilon_k(t) \hat{z}$. Here, $\Xi_k(t), \Upsilon_k(t)$ are real-time-dependent functions of momenta and are described by system-specific Hamiltonian parameters. Substituting into (1), the full Hamiltonian is expanded as:

$$H(t) = \sum_{k,-k} \left[\Upsilon_k(t) \left(c_k^\dagger c_k + c_{-k}^\dagger c_{-k} \right) + \Xi_k(t) \left(c_k^\dagger c_{-k}^\dagger + c_{-k} c_k \right) \right]. \quad (2)$$

The Hamiltonian in 2 can be rewritten in terms of Bogoliubov quasiparticles [70–72] (Bogolons) that are annihilated by fermionic operators γ_k , where

$$\begin{aligned} \gamma_k &= c_k \cos \varkappa_k + c_{-k}^\dagger \sin \varkappa_k, \\ \gamma_{-k} &= c_{-k} \cos \varkappa_k - c_k^\dagger \sin \varkappa_k, \end{aligned} \quad (3)$$

with $\tan(2\varkappa_k) = \Xi_k/\Upsilon_k$. Substituting into Eqs. (3) and (2) yields

$$H = \sum_{k,-k} \bar{E}_k \left(\gamma_k^\dagger \gamma_k + \gamma_{-k}^\dagger \gamma_{-k} - 1 \right) \quad (4)$$

with energy eigenvalues $\bar{E}_k = \sqrt{\Upsilon_k^2 + \Xi_k^2}$. Thus, the Hamiltonian conserves the Bogolon number at each momentum, given by the observable $\gamma_k^\dagger \gamma_k$: $[H, \gamma_k^\dagger \gamma_k] = 0$. This yields an extensive set of independent conserved quantities $\{\gamma_k^\dagger \gamma_k \ \forall k \in \text{FBZ}\}$ for half of the FBZ, one for each positive k . Hence, the Hamiltonian is integrable, as it can be described as an ideal gas of Bogolons that scatters without diffraction [73].

Now, suppose that the time dependencies are chosen in such a way that the matrix H_k alternates between two matrices $|H_1|_k$

and $|H_2|_k$ with time period T (frequency $\omega = 2\pi/T$) and 50% duty cycle, where

$$\begin{aligned} |H_1|_k &= (g_0 - b_k) \left(c_k^\dagger c_k + c_{-k}^\dagger c_{-k} \right) + \Delta_k \left(c_k^\dagger c_{-k}^\dagger + \text{h.c.} \right) \\ |H_2|_k &= g_1 \left(c_k^\dagger c_k + c_{-k}^\dagger c_{-k} \right). \end{aligned} \quad (5)$$

The Hamiltonian consists of two parts: (1) free-fermion terms $c_k^\dagger c_k$ that provide kinetic energies $g_0 - b_k$ for half the period, producing a group velocity dispersion b'_k and a flat-band dispersion without group velocity g_1 for the other half; (2) strongly correlated Cooper pair terms $c_k^\dagger c_{-k}^\dagger$ with their Hermitian conjugates, involving interaction energy Δ_k for half the period. If the symmetry-breaking field amplitude g_0 ensures a momentum k_0 where $g_0 = b_{k_0}$ and ω gives enough time for $|H_1|_{k_0}$ to generate a Cooper pair state from vacuum at the momentum $\pm k_0$ given by $|k_0, -k_0\rangle = c_{k_0}^\dagger c_{-k_0}^\dagger |0\rangle$, two criteria must be met.

$$g_0 = b_{k_0}, \quad \text{and} \quad \omega = 2\Delta_{k_0}. \quad (6)$$

At time $t = T/2$ immediately following the first duty cycle, a Cooper pair with momenta $\pm k_0$ materializes from vacuum due to the action of the Hamiltonian $|H_1|_{k_0}$. This state then experiences ballistic evolution through the second duty cycle under $|H_2|_{k_0}$ until $t = T$. In the subsequent period, the pair is annihilated by $|H_1|_{k_0}$ at $t = 3T/2$, initiating another ballistic transition of the resulting vacuum with $|H_2|_{k_0}$ until $t = 2T$. This sequence repeats, returning the system to its original state at every $2T$, characterized by a subharmonic response at $\pm k_0$ with a frequency half that of the driving frequency [65]. If observations were made at multiples of T , the Hamiltonian would seem stationary as the system cyclically forms and disintegrates a Cooper pair at $\pm k_0$. This behavior defines a DTC phase in which the temporal Z_2 symmetry is spontaneously broken.

To ensure that the phase remains rigid and impervious to microscopic changes within the system parameters, it is imperative that equations (6) consistently produce a solution within the Hamiltonian parameter space $|H_1|_k$ for any arbitrary selection of drive parameters g_0, ω . Consequently, this phase will rapidly deteriorate if $|H_1|_k$ is characterized by the absence of additional parameters, given that the two equations will only produce a singular solution of ω for any value of g_0 , leading to a rapid degradation of the subharmonic if ω slightly deviates from this value. However, the inclusion of one or more additional parameters will ensure the existence of infinite solutions for any selection of g_0 , thus merely causing k_0 to change minimally should ω be adjusted. The transverse field Ising model (TFIM) in a spin chain of length N with nearest-neighbor Heisenberg exchange interactions showcases a single-parameter scenario. The Hamiltonian

$$H = 2 \sum_{i=0}^{N-1} \left(g_0 \hat{S}_i^x + \hat{S}_i^z \hat{S}_{i+1}^z \right), \quad (7)$$

is described by vector operators \hat{S}_i , which capture the quantum mechanics of spin-1/2 particles or qubits, modeling systems

like quantum simulators [54, 74] with Josephson junctions [75] and gas microscopes with trapped ultra-cold ions [55, 76, 77] to mesoscopic ferromagnets [78, 79] and quantum cellular automata [80, 81]. The transverse field g_0 breaks the spatial Z_2 symmetry of the exchange interaction $\hat{S}_i^z \hat{S}_{i+1}^z$ and is expressed relative to the exchange energy, scaled to unity. Using a Jordan-Wigner transformation [82–87], this Hamiltonian transforms to $|H_1|_k$ with $b_k = \cos k$, $\Delta_k = \sin k$ and g_0 as the sole parameter. Subharmonic patterns in $\pm k_0$ quickly degrade, but this issue is addressed in [65] by extending to higher dimensions where $|H_1|_k$ emerges from a hexagonal spin network (also known as the Kitaev model [88–90]) with $b_k = \cos k_x + \cos k_y$, $\Delta_k = \sin k_x + \sin k_y$, employing the additional component of the now vectorized momentum $\mathbf{k} = k_x \hat{x} + k_y \hat{y}$ as a new parameter. We now explore the alternative, which involves the inclusion of more exotic one-dimensional spin-spin interactions, to introduce the required additional parameters without expanding dimensionally. For example, the Hamiltonian

$$H = 2 \sum_{i=0}^{N-1} \left(g_0 \hat{S}_i^x + \hat{S}_i^z \hat{S}_{i+1}^z + \lambda \hat{S}_{i-1}^z \hat{S}_i^x \hat{S}_{i+1}^z \right) \quad (8)$$

models the additional roles of longer-range interactions. The first term is the transverse field, the second is the nearest-neighbor Heisenberg exchange, and the third is a 3-body interaction with strength λ that can be used to model longer-range interactions that arise in quantum wires [91, 92]. The Jordan-Wigner transformation yields $|H_1|_k$ with $b_k = \cos k + \lambda \cos 2k$, $\Delta_k = \sin k + \lambda \sin 2k$. The Hamiltonian $|H_1|_k$ now contains two parameters, g_0 and λ , which can be adjusted independently. The Bogolon energies $E_k(g_0, \lambda) = \sqrt{[g_0 - b_k(\lambda)]^2 + \Delta_k^2(\lambda)}$ for the pair $k, -k$ are the eigenvalues, as can be inferred by comparing them with Eq. (4). Detailed profiles of the diagram of the equilibrium phase are discussed in [92, 93]. In the driven case, the additional parameter λ allows the introduction of new solutions to equations (6) for any given g_0, ω , ensuring that the time crystal phase remains rigid.

The dynamics induced by the driving protocol that alternates between $|H_1|_k$ and $|H_2|_k$ can now be studied to obtain the time crystal phase in a 2-parameter space of g_0, λ , whose phase profile we will explore in Sect. III. Quantum Floquet theory provides a powerful framework for analyzing this dynamics due to the presence of the time-periodic drive with period T and frequency ω (see [87, 94] and the references therein). If the quantum system is closed, then the central object is the propagator for multiple periods $U(nT) = \mathcal{T} \exp\left(-i \int_0^{nT} dt' H(t')\right)$, where \mathcal{T} denotes time ordering, and $H(t')$ is the full time-dependent Hamiltonian. As a consequence of Floquet's Theorem, $U(nT)$ can be decomposed as $U(nT) = e^{-i\bar{K}(nT)} (e^{-iH_F T})^n$, where $K(t)$ is the micromotion operator [95] with period T satisfying $K(t+T) = K(t)$ and can be set to vanish at $t = nT$ without loss of generality. In addition, H_F is the time-independent Floquet Hamiltonian (also called the effective Hamiltonian). This decomposition allows the stroboscopic

dynamics at integer multiples of the driving period to be governed by the simple exponential $U(nT) = (e^{-iH_F T})^n$, while the micromotion operator $K(t)$ captures the intra-period oscillations. The Floquet Hamiltonian eigenvalues Ω_α (quasienergies) are defined modulo ω , and the corresponding Floquet states $|\Psi_\alpha(t)\rangle = e^{-i\Omega_\alpha t} |\Phi_\alpha(t)\rangle$ evolve as Bloch waves in time, where $|\Phi_\alpha(t)\rangle$ are the T -periodic Floquet modes.

Floquet's Theorem can be applied to each distinct local $k, -k$ sector within this integrable system. Here, the time evolution is determined by the sector Hamiltonian $H_k(t)$, as specified in Eq. (1). The respective alternating Hamiltonians $|H_{1,2}|_k$ in Eqs. (5) can be associated with sector Hamiltonians $H_k^{(1)}(g_0, \lambda)$ and $H_k^{(2)}(g_1)$ through the Nambu spinor representation.

$$\begin{aligned} H_k^{(1)}(g_0, \lambda) &= E_k(g_0, \lambda) \mathbf{n}_k(g_0, \lambda) \cdot \boldsymbol{\tau} \\ H_k^{(2)}(g_1) &= g_1 \tau_3. \end{aligned} \quad (9)$$

Here, $\mathbf{n}_k(g_0, \lambda)$ is a unit vector on the surface of a Bloch sphere, given by the equation

$$\begin{aligned} \mathbf{n}_k(g_0, \lambda) &\equiv n_{1k}(g_0, \lambda) \hat{x} + n_{3k}(g_0, \lambda) \hat{z} \\ &= \frac{\Delta_k(\lambda) \hat{x} + [g_0 - b_k(\lambda)] \hat{z}}{E_k}. \end{aligned} \quad (10)$$

Applying Floquet's theorem yields the propagator in each sector at times $t = nT$ to be

$$U_k(nT) \equiv \left[e^{-iH_k^{(2)}(g_1)T/2} e^{-iH_k^{(1)}(g_0, \lambda)T/2} \right]^n = \left(e^{-iH_k^F T} \right)^n, \quad (11)$$

where H_k^F is the Floquet Hamiltonian corresponding to $H_k(t)$. Now, if we denote the eigenvalues by $\pm\theta_k/T$, then we can write

$$H_k^F \equiv \frac{1}{T} \theta_k(g_0, \omega, \lambda) \mathbf{h}_k(g_0, \omega, \lambda) \cdot \boldsymbol{\tau}, \quad (12)$$

where $\mathbf{h}_k(g_0, \lambda, g_1)$ is the unit vector on the surface of the Bloch sphere that describes the Floquet Hamiltonian in this particular sector. Finally, substituting the RHS of Eq. (12) into the RHS of Eq. (11) and comparing the traces on both sides after substituting Eqs. (9) into the LHS yields $\cos \theta_k = \text{Re}\{A_k\}$, where

$$\begin{aligned} A_k(g_0, \omega, \lambda) &= e^{-ig_1 T/2} \left\{ \cos \left[\frac{E_k(g_0, \lambda) T}{2} \right] \right. \\ &\quad \left. - in_{3k}(g_0, \lambda) \sin \left[\frac{E_k(g_0, \lambda) T}{2} \right] \right\}. \end{aligned} \quad (13)$$

From Eqn. (13), it can be seen that gaplessness occurs when $\text{Re}\{A_k\} = 1$, or

$$\begin{aligned} &\cos \left[\frac{g_1 T}{2} \right] \cos \left[\frac{E_{k_g}(g_0, \lambda) T}{2} \right] \\ &- \left[\frac{g_0 - b_{k_g}(\lambda)}{E_{k_g}(g_0, \lambda)} \right] \sin \left[\frac{g_1 T}{2} \right] \sin \left[\frac{E_{k_g}(g_0, \lambda) T}{2} \right] = 1. \end{aligned} \quad (14)$$

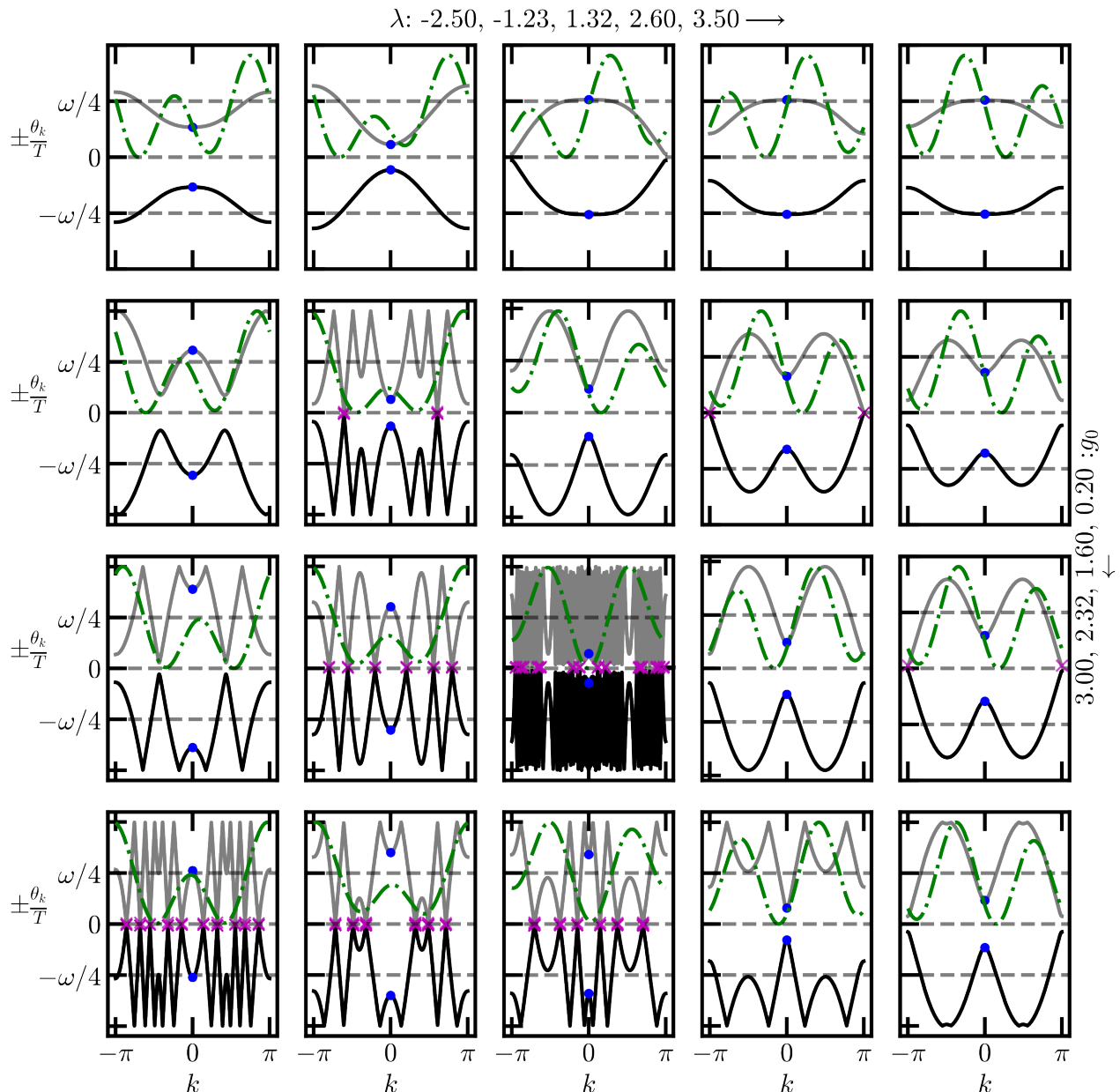


FIG. 1. Floquet quasienergies $\pm\theta_k$ (in units of time period T) derived from Eqn. (13). Each row corresponds to a fixed value of g_0 , while different values of λ are systematically displayed across columns. The values of g_0 and λ are clearly indicated above the topmost panels and after the rightmost panels, respectively. The values of $\pm\theta_k$ at the high-symmetry gapless point (non high-symmetry gapless points) are indicated by blue (magenta) colored dots. Additionally, the parameter $g_1 = 2\omega$, and ω has been optimized according to the cost function in Eqn. (21). Finally, the cost function itself has been plotted using green dot-dashed lines, with the ordinate values on the right axis (arbitrary units) in each panel. A subharmonic response exists only when a minimum in the cost function touches 0, and the quasienergy curves intersect $\pm\omega/4$ at the same value of k .

Additionally, the subharmonic mode appears in the quasienergy spectrum at momenta k_0 when Eq. (6) is satisfied, giving $\theta_{k_0}/T = \pm\omega/4$. Finally, we define equilibrium resonance by the condition $g_1 = 2n\omega$ (with integer n), Eq. (14) then reduces to $\cos [E_{k_g}(g_0, \lambda)T/2] = 1$, i.e. $E_{k_g}(g_0, \lambda) = 2n\omega$, which for $n = 0$ coincides with the equilibrium gapless points.

III. RIGIDITY AND PHASE DIAGRAM OF THE TIME CRYSTAL

The rigidity of the time crystal phase can be enforced by the additional parameter λ in the Hamiltonian $|H_1|_k$, which allows the existence of solutions to equations (6) for any arbitrary choice of g_0, ω . When the integrable time-crystal paradigm is implemented in spin-chain systems, the existence of bounds on

the right-hand side of these equations implies the presence of regions in parameter space where real solutions cease to exist. Crossing these boundaries induces phase transitions from the DTC to an alternative phase, as has been observed in similar systems. [65, 93] This section explores the phase diagram of the time crystal in the two-parameter space of g_0, λ for certain values of g_1, ω . The phase diagram is constructed by analyzing the quasienergy spectrum $\pm\theta_k$ derived from Eq. (13), as well as the DTC conditions in Eqs. (6) and identifying regions where stable subharmonic modes exist.

Analytical Phase Diagram

We apply the DTC conditions derived in Sect. II to the long-range spin chain parameterised by (g_0, λ) . The subharmonic (period-doubled) requirement for a momentum sector k is as follows.

$$\begin{aligned} f(k; g_0, \lambda) &= g_0 - b_k(\lambda) = 0, \\ \omega(k; \lambda) &= 2\Delta_k(\lambda), \end{aligned} \quad (15)$$

with

$$b_k(\lambda) = \cos k + \lambda \cos 2k, \quad \Delta_k(\lambda) = \sin k + \lambda \sin 2k. \quad (16)$$

For fixed λ the first equation admits real solutions only when

$$g_0 \in B_\lambda \equiv \left[\min_k b_k(\lambda), \max_k b_k(\lambda) \right], \quad (17)$$

so that the admissible region in the (g_0, λ) -plane is the filled set swept out by $b_k(\lambda)$.

To obtain B_λ explicitly, it is convenient to set $x = \cos k$, so

$$b(x; \lambda) = -2\lambda x^2 + x + \lambda, \quad x \in [-1, 1]. \quad (18)$$

The critical points satisfy $b'(x) = 0$, giving $x^* = (4\lambda)^{-1}$, which lies in $[-1, 1]$ only for $|\lambda| \geq 1/4$. Evaluating b at the boundary and at x^* yields

$$b(\pm 1) = \pm 1 - \lambda, \quad b(x^*) = \lambda + \frac{1}{8\lambda} \quad (|\lambda| \geq 1/4).$$

Hence,

- for $|\lambda| < 1/4$ there is no interior extremum and

$$B_\lambda = [-1 - \lambda, 1 - \lambda],$$

- for $|\lambda| \geq 1/4$ the interval endpoints are the extrema among $\{b(-1), b(1), b(x^*)\}$.

The Floquet quasienergy gaplessness condition (Eq. (14)) can be analyzed in parallel. At the high-symmetry point $k = 0$ (where $\Delta_0 = 0$) Eq. (14) reduces to a family of planes in the parameter space,

$$g_0 = \lambda - g_1 \pm 1 - 2n\omega, \quad n \in \mathbb{Z}, \quad (19)$$

whereas non-high-symmetry solutions (non-trivial roots of $\Delta_k = 0$) produce the complementary set

$$g_0 = -\lambda - g_1 \pm 1 + 2n\omega. \quad (20)$$

Under the equilibrium–resonance condition $g_1 = 2m\omega$, the Floquet gapless points collapse onto the equilibrium gapless manifold specified by $E_k(g_0, \lambda) = 2n\omega$ and consequently closely track the boundaries of B_λ . Deviations occur solely due to the $O(1/\lambda)$ contribution in $b(x^*)$ for small $|\lambda|$, such that the boundary of the B_λ manifold asymptotically converges to the equilibrium gapless manifold.

Taken together, these analytic results provide a compact criterion for the existence of subharmonic solutions: a given (g_0, λ) admits a DTC sector whenever $g_0 \in B_\lambda$ and the corresponding Floquet gap is open at the momentum solving Eq. (15). In contrast, crossing the gapless planes in Eqs. (19)–(20) signals the closing of the protecting quasienergy gap and marks the approximate boundary between the DTC and Floquet-paramagnetic regimes.

We now examine the structure of the time-crystal phase in greater detail. In Ref. [65], it was shown that the line $\lambda = 0$ cannot host a stable time crystal: with only a single tunable parameter in $|H_1|_k$, there exists at most one drive frequency ω satisfying the DTC conditions for a given g_0 , rendering the subharmonic response highly sensitive to small detunings of ω . Even for $\lambda \neq 0$, some residual sensitivity is expected. One practical strategy to mitigate this is to employ a hybrid quantum–classical variational loop in which a classical optimizer measures the relevant observables, evaluates a cost function, and updates the control parameters (k, ω) accordingly. Such closed-loop control can stabilize parameter regions that would otherwise be fragile under fixed drives [96].

Specifically, we optimize the pair (k, ω) by minimizing the cost function

$$F(k, \omega) = \left[g_0 - b_k(\lambda) \right]^2 + \left[\frac{\omega}{2} - \Delta_k(\lambda) \right]^2. \quad (21)$$

Minimization over ω is immediate and yields $\omega = 2\Delta_k(\lambda)$, reducing the problem to a single-variable objective,

$$F(k) = \left[g_0 - b_k(\lambda) \right]^2.$$

Any root of $f(k; g_0, \lambda) = 0$ is a global minimizer. Generically, this equation admits two solutions $k = \pm k_0$; when $|\lambda| \geq 1/4$, up to four solutions may exist. The map $(g_0, \lambda) \mapsto k$ is therefore multivalued, and a local optimizer initialized stochastically will converge to the minimum within its basin of attraction. Small perturbations in (g_0, λ) or in the initial guess can cause the optimizer to jump between equivalent minima, producing apparent discontinuities in the optimized k . This effect is most pronounced near $g_0 = -\lambda$, where $k = \pm\pi/2$ are exact solutions that produce $\omega = \pm 1$ at the same cost. Below this line, the solver alternates between these degenerate branches. Sufficiently far above, minima near $k \approx 0$ or π dominate, and a single branch yields a well-defined DTC subharmonic whenever the cost vanishes.

Figure 2 displays the filled set B_λ in the (g_0, λ) plane together with the Floquet gapless points for $g_1 = 2\omega$. The shaded regions delineate parameters that support subharmonic solutions (DTC) and those that do not (FPM), providing a transparent phase diagram of the driven system. The nonequilibrium phase structure can also be read directly from Fig. 1,

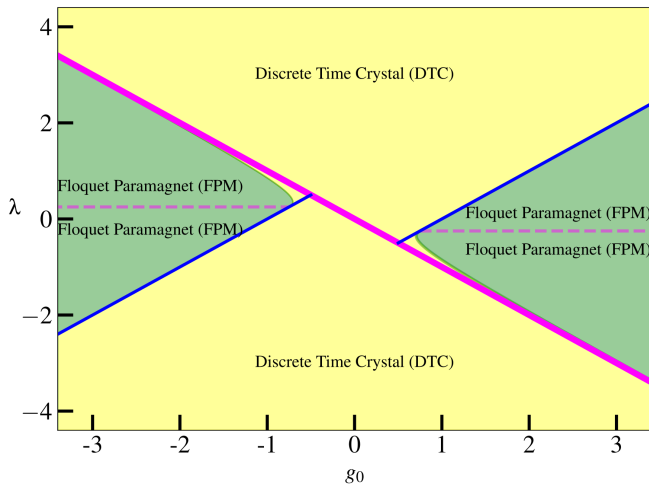


FIG. 2. Phase Diagram of the driven chain. The filled region B_λ (shaded yellow/light yellow and labeled "Discrete Time-Crystal (DTC)") in the (g_0, λ) plane marks parameters that admit subharmonic solutions. Regions outside this area (shaded green and labeled "Floquet paramagnet (FPM)") do not support subharmonic roots. Solid lines show the analytically determined Floquet gapless points [Eqs. (19) and (20)] for $g_1 = 2\omega$, with blue (magenta) lines indicating gaplessness at HS (non-HS) momenta. These gapless curves closely track the boundaries of B_λ and thus serve as approximate phase boundaries between the DTC and FPM regimes. Finally, the horizontal dashed lines at $|\lambda| = 1/4$ divide the two regions of B_λ with one or no interior extrema.

which shows the Floquet quasienergy spectra $\pm\theta_k$ for representative pairs (g_0, λ) alongside the corresponding cost-function profiles. Each row corresponds to a fixed g_0 , with λ varying between columns. The dashed horizontal lines at $\theta_k/T = 0, \pm\omega/4$ serve as reference scales. Blue dots and magenta crosses mark gapless points at high-symmetry (HS) and non-HS momenta, respectively; green dot-dashed lines show the cost function (right axis). In the FPM phase, the cost function does not vanish for any $k \neq 0$; if a zero occurs, it does so at $k = 0$ where $\omega = 0$, which does not produce no subharmonic. In the DTC regime, on the contrary, the cost function attains a zero minimum at some $k_0 \neq 0$, and the quasienergy curves cross $\pm\omega/4$ at the same k_0 , confirming the presence of a subharmonic mode.

The role of the Floquet gap as a diagnostic of phase transitions is equally apparent in Fig. 1: subharmonic solutions emerge as soon as the Floquet gapless points are crossed and the protecting gaps open. The gapless points therefore partition the (g_0, λ) plane into regions that support or do not support stable subharmonic solutions. The admissible region closely coincides with B_λ , while the complementary region exhibits paramagnetic behavior. Consequently, the analytically obtained gapless points serve as approximate phase boundaries separating the DTC and FPM regimes.

Numerical Phase Diagram

We complement the analytical phase diagram with a numerical survey of the parameter plane (g_0, λ) . This approach simultaneously provides an independent validation of the analytical predictions and offers a systematic means to identify additional physics that may not be captured by purely analytical considerations. Furthermore, numerical evaluations of the matrix elements of suitably chosen observables will elucidate the distinctions between the two phases and will characterize the emergence of off-diagonal long-range order in the DTC phase.

At each point on the (g_0, λ) grid, we numerically optimize subharmonic conditions to identify candidate pairs (k_0, ω) and evaluate stroboscopic diagnostics such as long-term average fidelity and two-point correlations. These calculations, implemented with robust minimization and spectral analysis routines, yield a comprehensive Floquet phase map that can be compared directly with the analytically obtained gapless points.

For every pair (g_0, λ) , we look for (k_0, ω) that minimizes the cost function in Eqn. (21). Minimization is performed using a trust-region method from the SciPy library [97], with numerical derivatives supplied by numdifftools [98]. An exact solution of Eqs. (15) corresponds to a zero minimum of the cost, in which case the sector fidelity

$$F_{k_0}(2nT) \equiv |\langle \psi_{k_0}(0) | \psi_{k_0}(2nT) \rangle|^2 \quad (22)$$

reaches unity. When no exact root exists, the minimizer returns a nonzero value and the stroboscopic fidelity at $2nT$ falls below unity, signaling melting of the time-crystalline order. Consequently, the long-time average $\bar{F}_{k_0}(2nT)$ (arithmetic mean over many even periods) is used as a primary diagnostic for the DTC phase; equivalently, $1 - \bar{F}_{k_0}(2nT)$ can be interpreted as the defect density in the k_0 sector [99]. All fidelity and dynamical observables reported here are computed using QuTiP [100].

Figure 3 (left panel) shows density plots of $\bar{F}_{k_0}(2nT)$, where ω is chosen at each point to minimize the cost function using the trust-region method; the overline denotes an average over long n . In addition, the parameter g_1 has been set to 2ω , the choice of equilibrium-resonance. By default, we choose to initialize the system in the fully polarized state $|\psi(0)\rangle = \bigotimes_i |\downarrow\rangle_i$, which is a ground state of the Hamiltonian when g_0 is large and negative. Thus, this figure shows the Floquet phase diagram in the (g_0, λ) plane. The time averages are taken over two-period intervals 10^4 ($T = 2\pi/\omega$). The regions with $\bar{F}_{k_0} \approx 1$ correspond to a time crystal (DTC): the system supports persistent stroboscopic subharmonic oscillations pinned at optimal momentum k_0 . The lower panels of Fig. 3 display the predictions of the trust-region algorithm for optimal ω and k_0 in the parameter space. These plots align closely with the analytical predictions in Sect. III, confirming the validity of the optimization approach. The time crystal phase (high \bar{F}_{k_0}) appears in the same regions where analytical DTC conditions are satisfied, while the FPM regime (variable \bar{F}_{k_0}) appears where no exact roots exist, except at the high-symmetry point $k_0 = 0$, where ω is trivially zero (see the bottom left panel of Fig. 3),

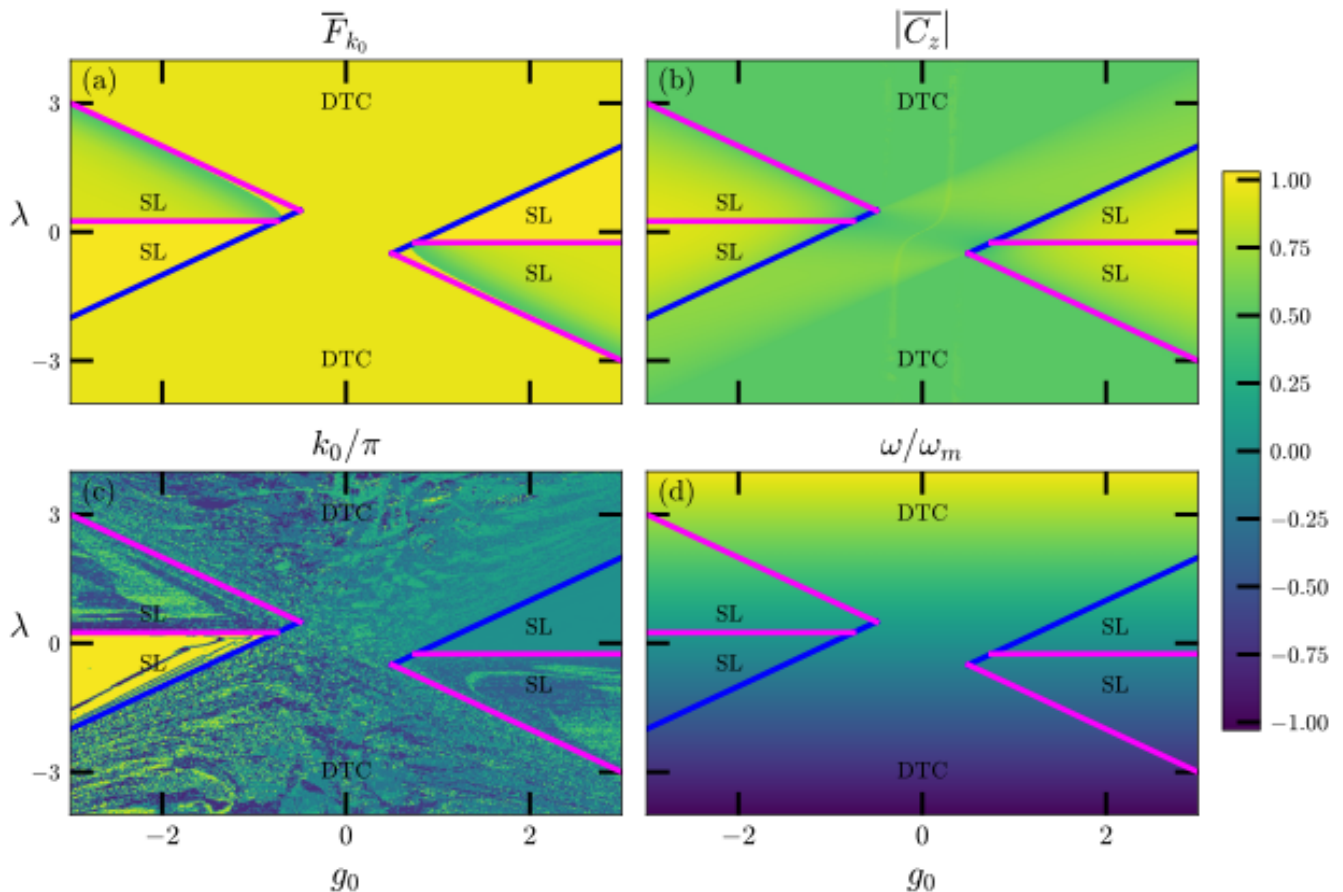


FIG. 3. Density plot of the long-time average (strobed at even multiples of T) of the fidelity \overline{F}_{k_0} at the optimal momentum k_0 (panel a), and the correlations \overline{C}_z (panel b), strobed at integer multiples of T . In panel b, the FBZ was discretized into $N = 1000$ equally spaced points between $-\pi$ and π , and k_0 explicitly included in the chosen sum. The time average is performed over 10^4 sets of $2T$ -intervals, where $T = 2\pi/\omega$. The parameter space is chosen to be g_0, λ . For each point, the value of ω is optimized using the trust-region method to minimize the cost function in Eqn. (21). The trust region predictions for k_0 (ω) are plotted in panels c (d). The parameter g_1 is set to 2ω , the equilibrium resonance condition described in the text. The solid lines indicate the gapless points in the Floquet quasienergy spectrum (Eqs. (19) and (20)), where the lines that correspond to gaplessness in the HS (non-HS) points are colored blue (magenta). The gapless points divide the parameter space into DTC and FPM phases, as labeled in the figure.

yielding spurious unit fidelity despite being in the FPM phase. The solid lines overlaying the plots are the analytically computed Floquet gapless points: blue lines indicate gaplessness at high-symmetry (HS) momenta and magenta lines indicate gaplessness at non-HS momenta. These gapless lines track the actual phase boundaries, with the $g_0 = -\lambda$ line converging to the phase boundary (given by the edges of the manifold B_λ in Eq. 17) in the asymptotic limit of large λ . Thus, when a quasienergy gap is open, a subharmonic can be pinned, and the DTC is stable; when that gap closes, the subharmonic can disappear, and the system falls into the FPM phase. In short, the existence and robustness of the time-crystalline phase are witnessed directly by where and how the Floquet quasienergy gaps open in momentum space. In addition, the lower panels of Fig. 3 show that the optimized ω varies smoothly throughout the phase diagram. This shows that tiny deviations of the actual drive frequency from its optimal value lead only to tiny changes in subharmonic momentum k_0 . In the continuum

limit ($N \rightarrow \infty$), this merely causes a slight displacement of the subharmonic response within the FBZ, rather than its complete destruction. A detector capable of resolving momentum-space dynamics would consistently observe a subharmonic at or close to k_0 , even when the drive frequency has small inaccuracies. Consequently, the smooth dependence signifies a Discrete Time Crystal that is robust against small perturbations in the thermodynamic (continuum) limit. The argument for rigidity is further supported by examining the full momentum-space dynamics at a fixed, non-optimized driving frequency, while varying other system parameters. Figure 4 shows density plots of the trace-norm of the unit-displaced propagator, $\|\mathbb{1} + U_k(2T)\|$ (with $U_k(2T)$ obtained from Eq. (11)), for fixed g_0, ω in the k, λ plane. This norm can vanish only at $k = k_0$, where $U_{k_0}(2T) = -1$, indicating the emergence of a subharmonic at that momentum. Using the operator norm is advantageous because the result is entirely independent of initial conditions. The parameter choices correspond to a generic

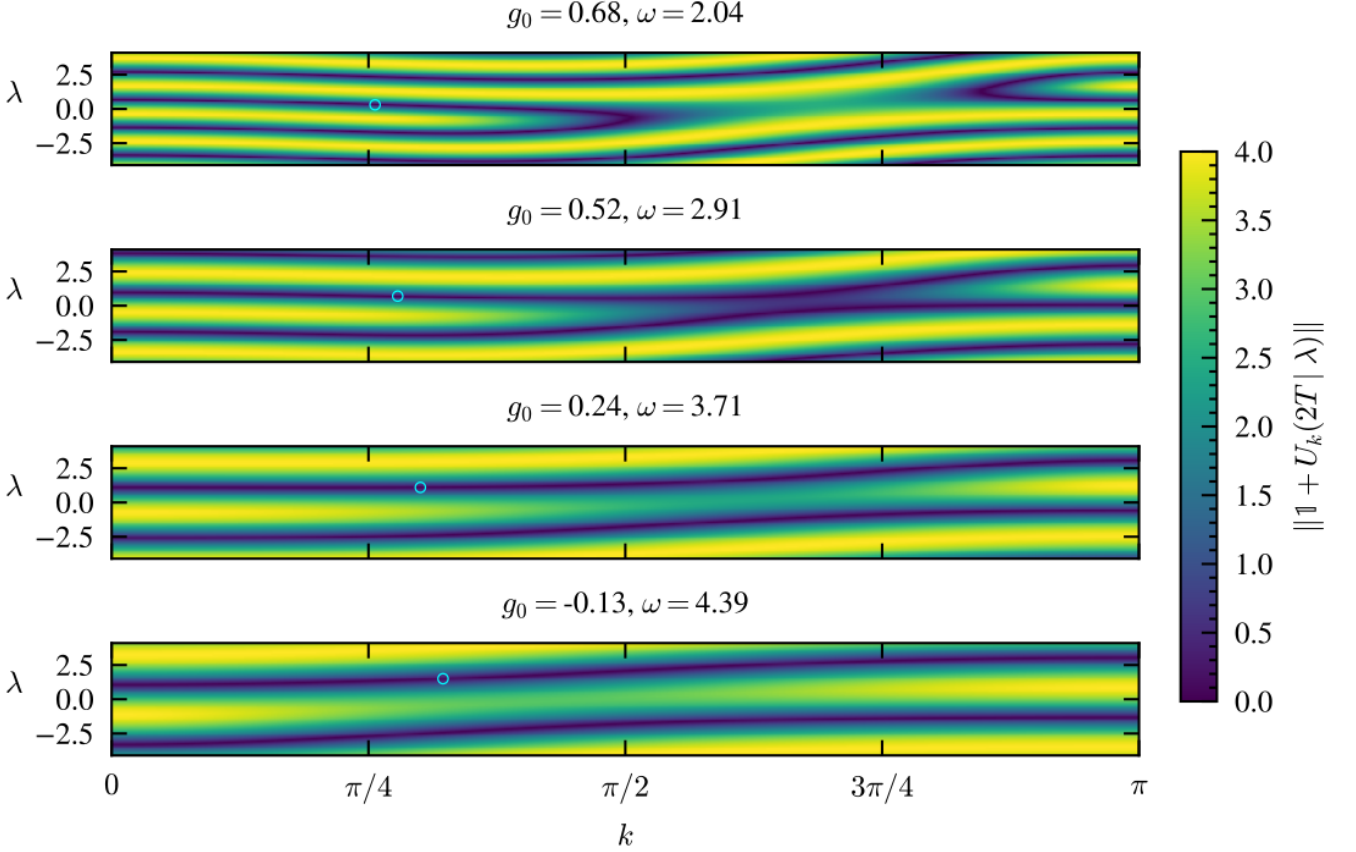


FIG. 4. Plots of $\|\mathbb{1} + U_k(2T)\|$, the trace of the unit-displaced propagator, in λ, k space, computed from QuTiP simulations. The fixed values of g_0, ω (indicated in the title of each panel) are chosen from a small cluster of values, and the parameter $g_1 = 2\omega$ is set to the equilibrium resonance condition. The driving frequency ω is not optimized. Nonetheless, the theoretically optimum k_0, λ point (where the subharmonic criteria in Eq. (6) are exactly met) is circled in cyan in each panel.

set of nearby points in the (g_0, ω) space, representing small variations. The theoretical k_0, λ location where the subharmonic criteria in Eqs. (6) are satisfied is marked. These plots clearly show that small parameter changes merely shift the subharmonic feature slightly to neighboring momenta within the FBZ. This behavior is consistent with the smooth dependence of k_0 on the parameters observed in the lower panels of Fig. 3, and further confirms the robustness of the time-crystalline phase against small perturbations in the drive frequency and other system parameters.

More physically measurable distinctions between these regions can be drawn by examining the full many-body temporal correlations. In the Heisenberg picture, these are given by

$$\begin{aligned} C_z(nT) &= \sum_i \langle \sigma_i^z(0) \sigma_i^z(nT) \rangle \\ &= \sum_i \langle \sigma_i^z e^{iH_F nT} \sigma_i^z e^{-iH_F nT} \rangle, \end{aligned} \quad (23)$$

where H_F is the full many-body Floquet Hamiltonian. The operator σ_i^z flips the spin at the site i , creating a pair of Bogolons with momenta $\pm k$ in each sector. The time evolution under H_F then causes these Bogolons to evolve independently, as

the Hamiltonian is integrable. The correlation function $C_z(n)$ can thus be expressed as a sum of the contributions from each momentum sector:

$$C_z(nT) = \frac{1}{N} \sum_k \langle \psi_k(0) | \exp\{iH_k^F \cdot nT\} \tau_3 \exp\{-iH_k^F \cdot nT\} | \psi_k(0) \rangle \quad (24)$$

where H_k^F is the Floquet Hamiltonian in the $k, -k$ sector shown in Eqn. (12), and $|\psi_k(0)\rangle = |0\rangle$ is the vacuum state in that sector.

The long-time average of $\overline{C_z}$, is plotted in the right panel of Fig. 3 and shows a phase manifold that is similar to that revealed by the fidelity analysis. The DTC region has a value of $\overline{C_z} \approx 0.5$, while the FTC region shows a slight increase in $\overline{C_z}$. In the FPM regions, the correlations show a marked increase from nearly half at the phase boundaries to nearly unity in regions with sufficiently large $|\lambda|$.

Off-Diagonal Long-Range Order

The nomenclature ‘‘Floquet Paramagnet’’ (FPM) and ‘‘Discrete Time Crystal’’ (DTC) is further justified by looking at the scaling behavior of the temporal off-diagonal long-range order (ODLRO) encoded in the antidiagonal elements of the temporal covariance matrix. Formally, we define the $N \times N$ temporal covariance matrix

$$\rho_{nm} = \langle \psi_{k_0}(0) | \tau_3(k_0, n) \tau_3(k_0, m) | \psi_{k_0}(0) \rangle, \quad (25)$$

$$\tau_3(k_0, n) \equiv U_{k_0}^\dagger(2nT) \tau_3 U_{k_0}(2nT),$$

where $U_{k_0}(T)$ is the Floquet propagator on the optimized (k_0, ω) given by eq. (11), and the stroboscopic time index n runs from $N/2$ to N . The anti-diagonal entries $\rho_{n, N-n}$ probe the maximal temporal separation between two spin-flip events. This quantity is an exact temporal analog of the off-diagonal spatial correlator $\langle a_n^\dagger a_m^\dagger a_n a_m \rangle$ at large spatial separation $|n - m|$ whose nonvanishing thermodynamic signals spatial ODLRO in superfluids and magnetic condensates [101, 102]. By averaging over these maximally separated pairs,

$$\overline{|\rho_{n, N-n}|} = \frac{1}{N} \sum_{n=N/2}^N |\rho_{n, N-n}|, \quad (26)$$

we construct a scalar diagnostic that is of the order of unity whenever long-range temporal order persists, and decays to zero in its absence.

Figure 5 plots the diagnostic in Eq. (26) as a function of $|\delta| = |g_0 + \lambda|/\sqrt{2}$, the Euclidean distance in the parameter space from the asymptotic critical line $\lambda = -g_0$, for points in the region $\delta < 0$. Most of this region consists of the FPM phase, although it also includes a small region of the DTC phase due to overlap with the exact B_λ -manifold described in the introduction to this section (also see Fig. 2).

The scaling laws revealed by this analysis furnish a precise temporal counterpart to the well-known ferromagnet-to-paramagnet transition in the quantum Ising chain. There, the spatial correlations $\langle \sigma_i^z \sigma_j^z \rangle$ decay algebraically $\sim |i - j|^{-\eta}$ at criticality, exponentially $\sim e^{-|i-j|/\xi}$ in the paramagnetic phase, and saturate to $m_s^2 \neq 0$ in the ferromagnetic phase, with m_s the spontaneous magnetization signaling spatial ODLRO [84, 103]. An entirely parallel structure emerges here in the temporal domain.

- (i) **DTC phase:** $\overline{|\rho_{n, N-n}|} = \mathcal{O}(1)$, signaling temporal ODLRO. The system remembers its initial spin polarization across arbitrarily many drive periods, the precise temporal analog of long-range ferromagnetic order.
- (ii) **Near the DTC-FPM critical boundary** ($|\delta| \lesssim 1$): a power-law collapse on the FPM side

$$\overline{|\rho_{n, N-n}|} \sim |\delta|^\alpha, \quad (27)$$

with good goodness-of-fit ($\alpha \approx -3.34$, $\chi^2/\text{dof} \approx 0.84$), mirrors the algebraic decay of correlations at a quantum critical point with anomalous dimension η . The

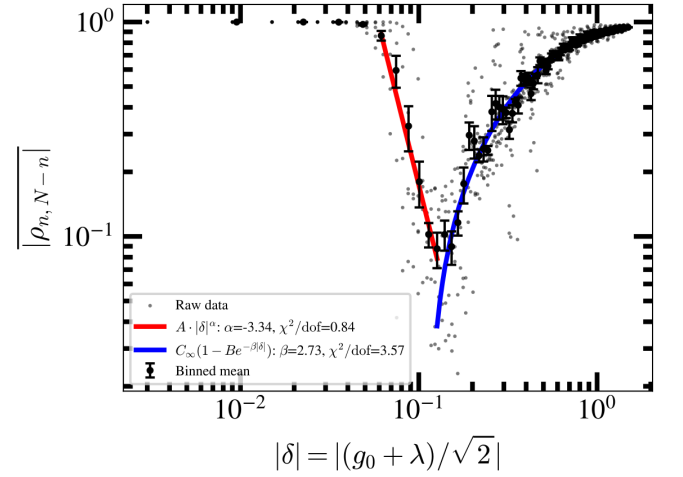


FIG. 5. Log-log plots of temporal correlations averaged over the anti-diagonal elements of the temporal covariance matrix ρ_{nm} , defined in Eq. (25). The panel plots $\overline{|\rho_{n, N-n}|}$ defined in Eq. (26) as a function of $|\delta|$, where $\delta = (g_0 + \lambda)/\sqrt{2}$ is the Euclidean distance from the line $\lambda = -g_0$. The raw data (small gray dots) is taken from an unordered set in the g_0, λ plane; only points with $\delta < 0$ are retained. For each such point, the temporal correlation series is obtained via QuTiP simulations with time steps of $2T$, truncated at $t = NT$ with $N = 100$. For each value of δ , all corresponding values of $\bar{\rho}$ from the relevant g_0, λ pairs are collected into histograms with 115 bins; the mean of each histogram is shown as a large black circle, and the error bars represent the standard deviation. In the Floquet Paramagnetic (FPM) regime, these binned means are fitted to the following scaling hypothesis: power-law collapse near criticality (red) and exponential growth in deep-FPM (blue). The fitted parameters and corresponding χ^2 values from the hypothesis tests are given in the legend.

divergence as $\delta \rightarrow 0^-$ reflects the diverging temporal correlation ‘‘length’’ (measured in units of the drive period) as the system approaches the phase boundary.

- (iii) **Deep FPM** ($|\delta|$ large): exponential saturation to a value strictly below unity,

$$\overline{|\rho_{n, N-n}|} \sim [1 - B e^{-\beta|\delta|}], \quad (28)$$

with a fitted growth rate $\beta \approx 2.73$, consistent with the exponential suppression of correlations deep in a conventional quantum paramagnetic phase, here manifested in the time domain. The absence of temporal ODLRO is the hallmark of a phase that has not broken the discrete-time-translation symmetry.

The extracted exponent $\alpha \approx -3.34$ ($\chi^2/\text{dof} \approx 0.84$) characterizes the critical singularity of the temporal ODLRO at the DTC-FPM transition; its deviation from standard transverse-field Ising exponents [104] suggests that either the composite nature of $\overline{|\rho_{n, N-n}|}$ as an observable or the integrability constraints of the Floquet drive modify the effective universality class, a question we leave for future investigation.

The crossover between regimes (ii) and (iii) locates the dynamical equivalent of the Ising correlation length ξ : within the FPM, this temporal correlation length is finite, just as a

paramagnet possesses only short-range spin correlations. In DTC, by contrast, the temporal correlation length diverges (signaled by the saturation of $|\rho_{n,N-n}|$ to $\mathcal{O}(1)$), exactly as the correlation length diverges in a ferromagnet. This triptych of scaling regimes—temporal ODLRO in the DTC, algebraic critical scaling at the boundary, and exponential paramagnetic suppression in the FPM—provides a rigorous temporal-order-parameter justification for both phase names, placing them on the same conceptual foundation as spontaneous symmetry breaking in equilibrium quantum magnets.

IV. FINITE-SIZE SCALING: METHODOLOGY AND RESULTS

A. Model and Parameter Selection

In order to look at finite-size effects, we study the system dynamics numerically for long times at finite sizes. A crucial point to note is the order of limits. In many-body physics, it is well known that the order of limits can significantly affect the results. For example, in the context of Anderson localization in one dimension, if one first takes the limit of the vanishing disorder strength $h \rightarrow 0$ and then considers the thermodynamic limit $N \rightarrow \infty$, one might incorrectly conclude that all states are delocalized. However, this conclusion is erroneous because the correct order of limits is to take $N \rightarrow \infty$ first, followed by $h \rightarrow 0$. This ensures that even an infinitesimal amount of disorder can localize states in an infinite system. For a detailed discussion on this matter as it pertains to Many Body Localization, see [12].

This means that in our scenario, we first select a pair of g_0, λ and then determine k_0, ω . However, this particular k_0 may not correspond to a reciprocal lattice point except in the limit of infinite size. For a finite system of size N , the reciprocal lattice point nearest to k_0 , denoted $k_0^R(N) = 2\pi n/N$ (where n varies with N), will only approximately optimize the cost function f in Eq. (21). It is expected that, for the $k_0^R, -k_0^R$ pair, the subharmonic will exhibit distortions with 'beats' (similar to those observed in [12]) at a frequency of $\delta\Omega(N) = k_0 - k_0^R(N)$. This process disrupts the time crystal with a beat period $t_b(N) \sim (\delta\Omega(N))^{-1}$. As N becomes very large, $\delta\Omega(N)$ is expected to decrease inversely with N , eventually disappearing as $N \rightarrow \infty$ for the DTC phase. For the FPM phase, the behavior is expected to be different, with $\delta\Omega(N)$ potentially stabilizing or even increasing with N . This would indicate the absence of any robust subharmonic response. Thus, the proposed DTC "resists infinitely at the thermodynamic limit", although the scaling of melting time is linear due to the integrable nature of this system, which contrasts with the exponential suppression of melting as is in the case of Many-Body Localized time crystals [5, 12, 105].

For each parameter point (g_0, λ) (chosen near putative critical points, deep DTC and spin-liquid-like regions), the pair (k_0, ω) is obtained numerically as described in Sect. III. In general, k_0 is incommensurate with lattice discretization for finite N , and so the nearest lattice momentum $k_0^R(N)$ is used

for time evolution.

$$k_0^R(N) = \arg \min_{2\pi n/N} |k - k_0|. \quad (29)$$

The mismatch $\delta k(N) = k_0 - k_0^R(N)$ induces a slow dephasing of the subharmonic response nominally locked at $\Omega = \omega/2$, producing a beat envelope and a splitting in the Fourier spectrum. The melting (dephasing) time satisfies $t_m(N) \sim 1/\delta\Omega(N)$, where $\delta\Omega$ is the frequency splitting. For each N (log-spaced from $\mathcal{O}(10^2)$ to $\mathcal{O}(10^4)$) we construct 2×2 unitaries U_1, U_2 for $k_0^R(N)$ with period $T = 2\pi/\omega$ and choose $g_1 = 2\omega$ (equilibrium resonance condition). Starting from the vacuum spinor, we evolve stroboscopically for the $2n_{\text{cycles}} + 1$ half-steps ($n_{\text{cycles}} = 10^5$), storing $C_z(k_0^R, nT)$. Computations employ GPU acceleration (CuPy [106]) and Python multiprocessing in N . The real-time series is then FFT-transformed. A two-Lorentzian model $L_1 + L_2$ (implemented by using lmfit [107]) fits $|\text{FFT}|$ near $\omega/2$, producing peak centers $\Omega_{1,2}$ and a melting frequency $\delta\Omega = |\Omega_1 - \Omega_2|$. After filtering ($\delta\Omega > \text{floor}$, finite values), the Random Sample Consensus (RANSAC) regression algorithm of the scikit-learn package [69] is applied to $\log \delta\Omega$ versus $\log N$ to extract a scaling exponent α from the model giving $\delta\Omega \sim N^\alpha$. Figure 6 shows the fitted spectra and scaling for several parameter points (panels labeled a-h, x, y), while Fig. 7 shows the corresponding time series $C_z(k_0^R, nT)$ for two lattice sizes. Both figures illustrate the different regimes observed.

B. Observed Regimes

The following regimes are revealed from the plots in Figs. 6 and 7:

- **Deep DTC (panels a,f,h):** Clear and persistent two-peak structure in the FFTs of Fig. 6; scaling exponent $\alpha \approx -1$ (algebraic decay). The time series in Fig. 7 further corroborate this identification, showing long-lived period-doubled oscillations with a finite-size beat envelope whose period grows with N . Hence, the suppression of melting is weaker than the exponential suppression observed for time crystals in non-integrable systems [5, 12, 105]. We anticipate that incorporating suitable 4-fermion perturbations, in analogy with the spin-orbit coupling introduced in 2D integrable time crystals discussed in [65], would enhance this suppression to exponential scaling, which we leave for future work.
- **FPM (panels c, d, g, j):** Spectral splitting deteriorates or plateaus, and the extracted α is unstable (RANSAC retains only a small inlier subset). Panel c in Fig. 7 shows rapid, low-amplitude oscillations with little dependence on N (the oscillatory FPM), while panels d and j show essentially stationary behavior (due to the subharmonic momentum k_0 being at an HS point). These behaviors contrast sharply with the DTC regimes, where the beat envelope period increases with N .

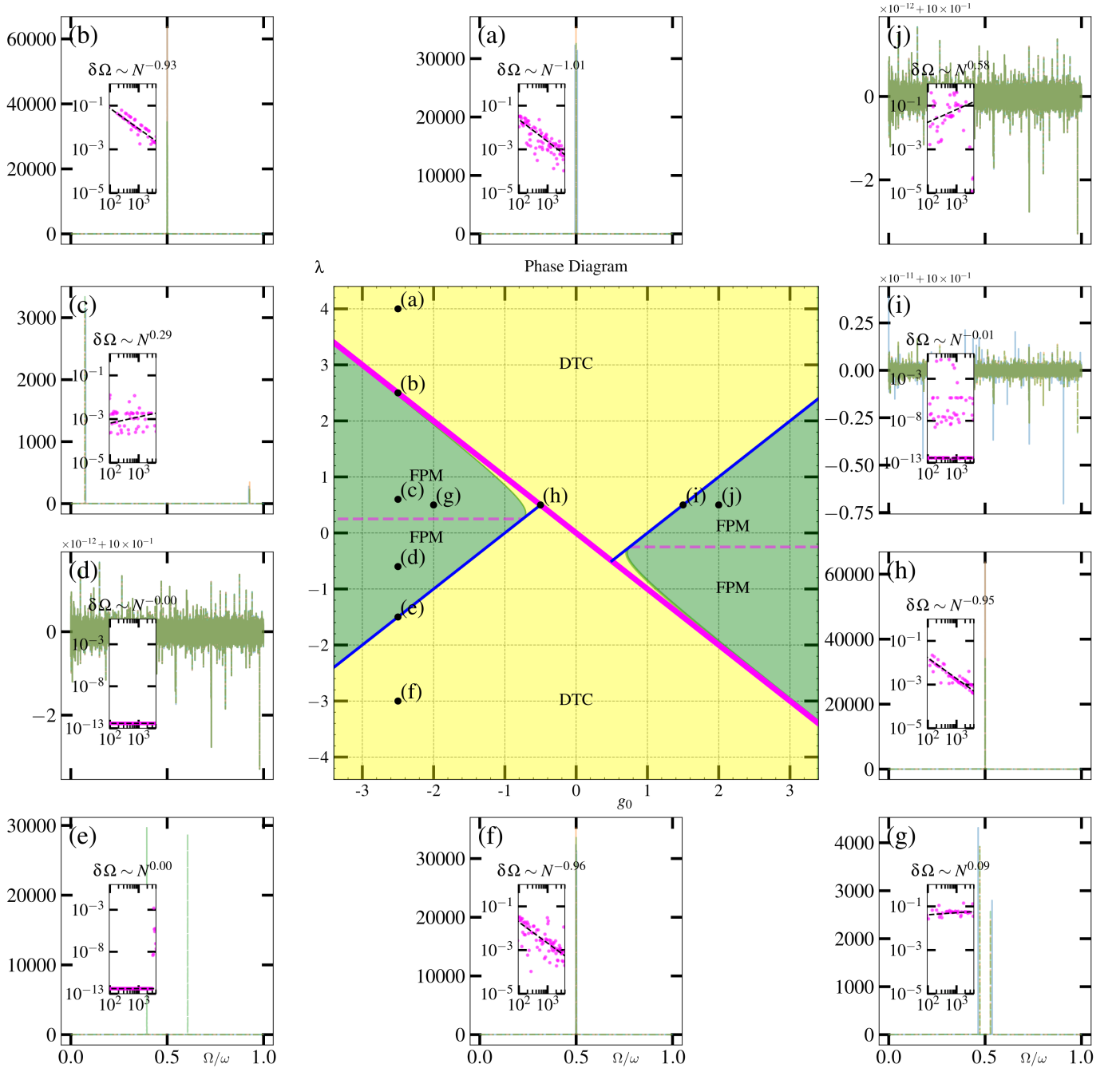


FIG. 6. Center: Full floquet phase diagram in the (g_0, λ) plane at equilibrium resonance $g_1 = 2\omega$, indicating regions of Discrete Time-Crystal (DTC, yellow) and Floquet Paramagnet (FPM, green). Solid blue and magenta lines mark analytically obtained Floquet gapless points at high-symmetry and non-HS momenta [Eqs. (19, 20)]. Black dots (marked a-j) identify parameter points used in the finite-size analysis. Surrounding panels in counter-clockwise order: normalized power spectra [FFT] of the stroboscopic subharmonic at the optimal momentum (with incommensurate k_0 replaced by its nearest lattice momentum $k_0^R(N)$) for several system sizes (solid traces: increasing N ; dashed verticals: fitted peak centers). Each panel reports the fitted scaling $\delta\Omega \sim N^\alpha$ obtained from the two-Lorentzian peak splitting $\delta\Omega = |\Omega_1 - \Omega_2|$; insets display the log-log data and the RANSAC fit.

- **On the asymptotic critical line $\lambda \approx -g_0$ (panel b):** Similar negative α on the DTC side.
- **On critical lines $\lambda = g_0 \pm 1$ (panels e,i):** Dependencies are highly sensitive to machine precision, with behavior

consistent with FPM appearing at small system sizes and large spectral splits at larger sizes without consistent scaling.

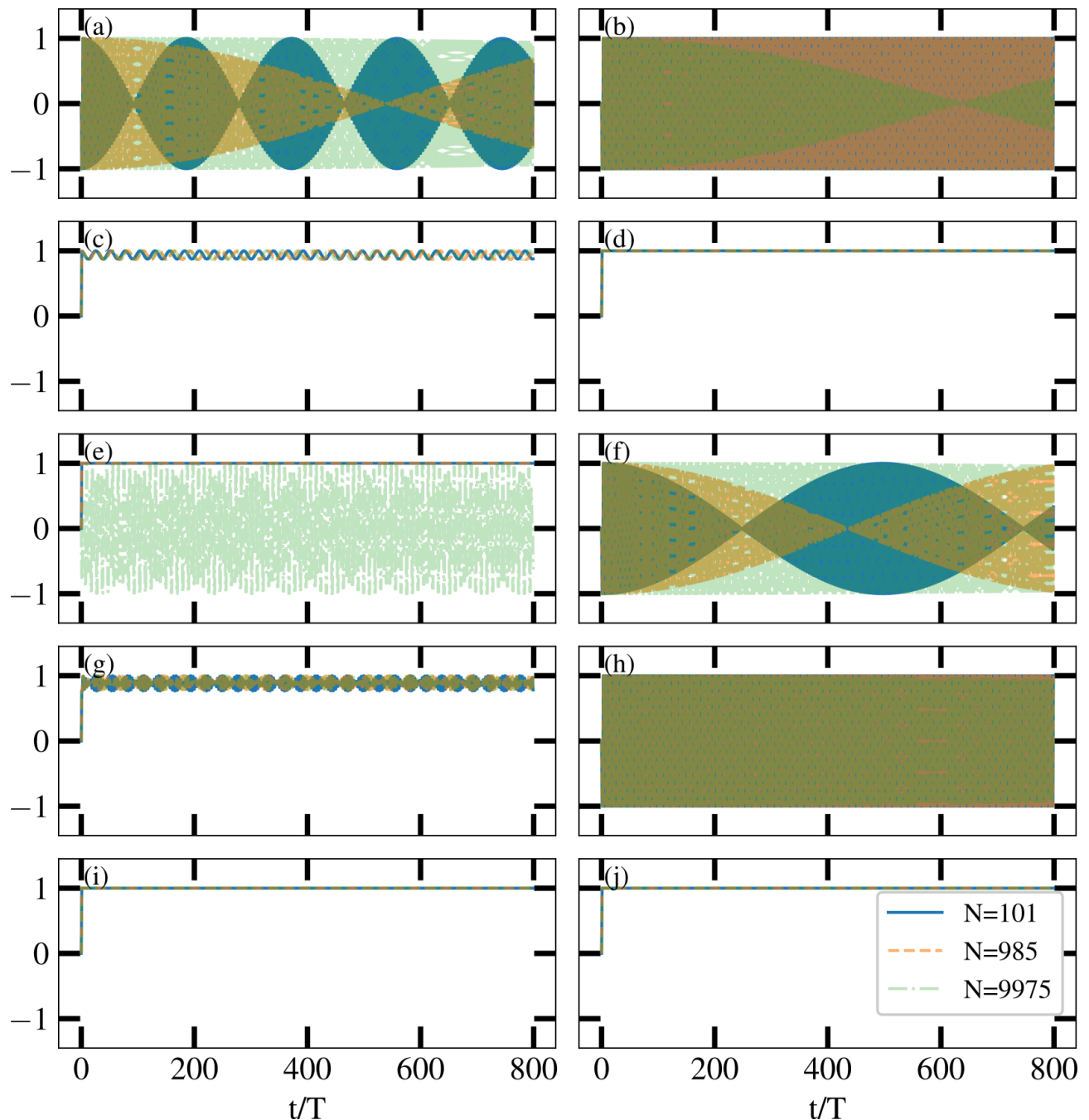


FIG. 7. Stroboscopic time series of $C_z(k_0^R, nT)$ (defined in Eq. (24)) at k_0^R , the lattice momentum nearest to the optimal k_0 , shown for three system sizes ($N \sim 100$: solid dark-cyan; $N \sim 1000$ dashed dark-orange, and $N \sim 10,000$; dash-dot lime-green). Panels where the parameters are deep in the DTC phase (a,f) display long-lived period-doubled oscillations with a finite-size beat envelope whose period grows with N (data shown up to $n = 800$ drive periods). Near-critical panels on the DTC side (b,h) show slower decoherence; and those on the FPM side (e,i) show mostly stationary behavior. The FPM at (c,g) has fast, low-amplitude oscillations, while the FPM at (d,j) is essentially stationary, illustrating how finite-size dephasing discriminates robust DTC scaling from FPM behavior.

V. CONCLUSION

In our study, we have identified a new Discrete Time-Crystal (DTC) phase within a class of one-dimensional quadratic lattice Hamiltonians subjected to periodic driving. The role of

integrability is crucial for generating the necessary subharmonics: it enables the decomposition of the Hilbert space into an extensive number of invariant momentum-space subspaces, which in turn facilitates subharmonic response at selected momenta. By analyzing the Floquet quasiparticle spectrum across the parameter space, we demonstrated how NNN

interactions open and control quasienergy gaps that pin these modes and suppress dephasing channels, stabilizing the DTC against melting in strictly one-dimensional spin chains. We further identified a Floquet paramagnetic regime and corroborated its nature with finite-size scaling of the subharmonic splitting. The finite-size analysis also revealed algebraic scaling in the suppression of melting, which is weaker than the exponential lifetimes in non-integrable systems such as MBL-stabilized DTCs. However, it should be noted that an analogous algebraic decay occurs in the higher-dimensional integrable systems analyzed in [65], where it was transformed into an exponential decay by the perturbative inclusion of non-integrable four-fermion coupling terms. We expect that comparable enhancements will occur in the one-dimensional systems investigated in the present work, a detailed analysis of which is deferred to future research.

These results fall in line with recent theoretical advances in integrable Floquet systems showing that algebraic integrability and engineered couplings can together stabilize time-crystalline order without disorder or prethermal fine-tuning. In particular, the NNN engineering we propose provides a concrete, experimentally accessible route to realize integrability-protected DTCs in one dimension. With the rapid development of programmable quantum simulators and superconducting-qubit platforms capable of tunable NNN couplings and variational control, the stabilization mechanism described here can be tested on Noisy Intermediate-Scale Quantum (NISQ)

devices, thereby linking exactly solvable theory to near-term experiments in synthetic quantum matter.

ACKNOWLEDGMENTS

RC and AR acknowledge the use of the BUParamShavak high-performance computing facility at the Department of Physics, The University of Burdwan, Bardhaman, India. SS acknowledges support from the Science and Engineering Research Board (SERB), India, through the Core Research Grant No. CRG / 2021 / 000996. MR thanks DST, India, for support through the DST/FFT/NQM/QSM/2024/3 project.

AUTHOR CONTRIBUTIONS

RC: Conceptualization, Data curation, Project administration, Software, Visualization, Writing – original draft; **MR:** Investigation, Resources, Validation, Writing – review & editing; **SM:** Resources, Validation, Visualization; **AR:** Conceptualization, Data curation, Project administration, Formal analysis, Investigation, Methodology, Resources, Software, Supervision, Visualization, Writing – original draft; **SS:** Conceptualization, Formal analysis, Funding acquisition, Investigation, Methodology, Supervision, Validation, Writing – review & editing;

-
- [1] F. Wilczek, Quantum Time Crystals, *Physical Review Letters* **109**, 160401 (2012).
- [2] A. Shapere and F. Wilczek, Classical Time Crystals, *Physical Review Letters* **109**, 160402 (2012).
- [3] P. Bruno, Comment on “Quantum Time Crystals”, *Physical Review Letters* **110**, 118901 (2013).
- [4] H. Watanabe and M. Oshikawa, Absence of quantum time crystals, *Physical Review Letters* **114**, 251603 (2015).
- [5] D. V. Else, B. Bauer, and C. Nayak, Floquet Time Crystals, *Physical Review Letters* **117**, 090402 (2016).
- [6] M. P. Zaletel, M. Lukin, C. Monroe, C. Nayak, F. Wilczek, and N. Y. Yao, Colloquium: Quantum and classical discrete time crystals, *Reviews of Modern Physics* **95**, 031001 (2023).
- [7] D. V. Else, C. Monroe, C. Nayak, and N. Y. Yao, Discrete time crystals, *Annual Review of Condensed Matter Physics* **11**, 467 (2020).
- [8] S. Choi, J. Choi, R. Landig, G. Kucsko, H. Zhou, J. Isoya, F. Jelezko, S. Onoda, H. Sumiya, V. Khemani, C. von Keyserlingk, N. Y. Yao, E. Demler, and M. D. Lukin, Observation of discrete time-crystalline order in a disordered dipolar many-body system, *Nature* **543**, 221 (2017).
- [9] J. Zhang, P. W. Hess, A. Kyprianidis, P. Becker, A. Lee, J. Smith, G. Pagano, I.-D. Potirniche, A. C. Potter, A. Vishwanath, N. Y. Yao, and C. Monroe, Observation of a discrete time crystal, *Nature* **543**, 217 (2017).
- [10] A. Kyprianidis, F. Machado, W. Morong, P. Becker, K. S. Collins, D. V. Else, L. Feng, P. W. Hess, C. Nayak, G. Pagano, N. Y. Yao, and C. Monroe, Observation of a prethermal discrete time crystal, *Science* **372**, 1192 (2021).
- [11] A. Pizzi, D. Malz, G. De Tomasi, J. Knolle, and A. Nunnenkamp, Time crystallinity and finite-size effects in clean floquet systems, *Physical Review B* **102**, 214207 (2020).
- [12] S. Liu, S.-X. Zhang, C.-Y. Hsieh, S. Zhang, and H. Yao, Discrete time crystal enabled by Stark many-body localization, *Physical Review Letters* **130**, 120403 (2023), 2208.02866.
- [13] R. Nandkishore and D. A. Huse, Many-Body Localization and Thermalization in Quantum Statistical Mechanics, *Annual Review of Condensed Matter Physics* **6**, 15 (2015).
- [14] J. Randall, C. E. Bradley, F. V. van der Gronden, A. Galicia, M. H. Abobeih, M. Markham, D. J. Twitchen, F. Machado, N. Y. Yao, and T. H. Taminiau, Many-body-localized discrete time crystal with a programmable spin-based quantum simulator, *Science* **374**, 1474 (2021).
- [15] D. Li, A. E. Dementyev, Y. Dong, R. G. Ramos, and S. E. Barrett, Generating unexpected spin echoes in dipolar solids with π pulses, *Physical Review Letters* **98**, 190401 (2007).
- [16] N. Y. Yao, A. C. Potter, I.-D. Potirniche, and A. Vishwanath, Discrete Time Crystals: Rigidity, Criticality, and Realizations, *Physical Review Letters* **118**, 030401 (2017).
- [17] A. Stasiuk and P. Cappellaro, Observation of a prethermal u(1) discrete time crystal, *Physical Review X* **13**, 041016 (2023).
- [18] D. Vu and S. Das Sarma, Dissipative prethermal discrete time crystal, *Physical Review Letters* **130**, 130401 (2023).
- [19] B. Krajewski, L. Vidmar, J. Bončič, and M. Mierzejewski, Restoring ergodicity in a strongly disordered interacting chain, *Physical Review Letters* **129**, 260601 (2022).
- [20] H. Ha, A. Morningstar, and D. A. Huse, Many-Body Resonances in the Avalanche instability of many-body localization, *Physical Review Letters* **130**, 250405 (2023).

- [21] S. Birnkammer, A. Bastianello, and M. Knap, Prethermalization in one-dimensional quantum many-body systems with confinement, *Nature Communications* **13**, 7663 (2022).
- [22] D. J. Luitz, R. Moessner, S. L. Sondhi, and V. Khemani, Prethermalization without temperature, *Physical Review X* **10**, 021046 (2020).
- [23] A. Pizzi, A. Nunnenkamp, and J. Knolle, Classical prethermal phases of matter, *Physical Review Letters* **127**, 140602 (2021).
- [24] F. Machado, D. V. Else, G. D. Kahanamoku-Meyer, C. Nayak, and N. Y. Yao, Long-range prethermal phases of nonequilibrium matter, *Physical Review X* **10**, 011043 (2020).
- [25] A. Santini, G. E. Santoro, and M. Collura, Clean two-dimensional floquet time crystal, *Physical Review B* **106**, 134301 (2022).
- [26] A. Pizzi, J. Knolle, and A. Nunnenkamp, Higher-order and fractional discrete time crystals in clean long-range interacting systems, *Nature Communications* **12**, 2341 (2021).
- [27] Z.-Y. Li and Y.-R. Zhang, Discrete time crystals in one-dimensional classical floquet systems with nearest-neighbor interactions (2025), arXiv:2505.07524 [quant-ph].
- [28] H. Keßler, J. G. Cosme, M. Hemmerling, L. Mathey, and A. Hemmerich, Emergent limit cycles and time crystal dynamics in an atom-cavity system, *Physical Review A: Atomic, Molecular, and Optical Physics* **99**, 053605 (2019).
- [29] R. Hurtado-Gutiérrez, F. Carollo, C. Pérez-Espigares, and P. I. Hurtado, Building continuous time crystals from rare events, *Physical Review Letters* **125**, 160601 (2020).
- [30] H. Keßler, P. Kongkhambut, C. Georges, L. Mathey, J. G. Cosme, and A. Hemmerich, Observation of a dissipative time crystal, *Physical Review Letters* **127**, 043602 (2021).
- [31] J. Wang, K. Sacha, P. Hannaford, and B. J. Dalton, Discrete time crystals in bose-einstein condensates and the symmetry-breaking edge in a simple two-mode theory, *Physical Review A: Atomic, Molecular, and Optical Physics* **104**, 053327 (2021).
- [32] J. Wang, P. Hannaford, and B. J. Dalton, Many-body effects and quantum fluctuations for discrete time crystals in bose-einstein condensates, *New Journal of Physics* **23**, 063012 (2021).
- [33] K. Bull, A. Hallam, Z. Papić, and I. Martin, Tuning between continuous time crystals and many-body scars in long-range xyz spin chains, *Physical Review Letters* **129**, 140602 (2022).
- [34] N. Maskara, A. A. Michailidis, W. W. Ho, D. Bluvstein, S. Choi, M. D. Lukin, and M. Serbyn, Discrete time-crystalline order enabled by quantum many-body scars: Entanglement steering via periodic driving, *Physical Review Letters* **127**, 090602 (2021).
- [35] W. Deng and Z.-C. Yang, Using models with static quantum many-body scars to generate time-crystalline behavior under periodic driving, *Physical Review B* **108**, 205129 (2023).
- [36] A. Chandran, T. Iadecola, V. Khemani, and R. Moessner, Quantum Many-Body Scars: A Quasiparticle Perspective, *Annual Review of Condensed Matter Physics* **14**, 443 (2023).
- [37] A. Pizzi, L.-H. Kwan, B. Evrard, C. B. Dag, and J. Knolle, Genuine quantum scars in many-body spin systems, *Nature Communications* **16**, 6722 (2025).
- [38] M. Rahaman, A. Sakurai, and A. Roy, Time crystal embodies chimeralike state in periodically driven quantum spin system, *New Journal of Physics* **26**, 063035 (2024).
- [39] M. Rahaman and A. Roy, Discrete time crystal order in spin-chains enabled by floquet flat-bands (2026), arXiv:2603.14307 [cond-mat.stat-mech].
- [40] A. Kshetrimayum, J. Eisert, and D. M. Kennes, Stark time crystals: Symmetry breaking in space and time, *Physical Review B* **102**, 195116 (2020).
- [41] T. Banerjee and K. Sengupta, Emergent conservation in the floquet dynamics of integrable non-hermitian models, *Physical Review B* **107**, 155117 (2023).
- [42] A. Haldar and A. Das, Statistical mechanics of floquet quantum matter: Exact and emergent conservation laws, *Journal of Physics: Condensed Matter* **34**, 234001 (2022).
- [43] V. Gritsev and A. Polkovnikov, Integrable floquet dynamics, *SciPost Physics* **2**, 021 (2017).
- [44] E. Vernier, H.-C. Yeh, L. Piroli, and A. Mitra, Strong zero modes in integrable quantum circuits, *Physical Review Letters* **133**, 050606 (2024).
- [45] M. Ž Žnidarič, U. Duh, and L. Zadnik, Integrability is generic in homogeneous $U(1)$ -invariant nearest-neighbor qubit circuits, *Physical Review B* **112**, L020302 (2025).
- [46] E. H. Müller, Exact conservation laws for neural network integrators of dynamical systems, *Journal of Computational Physics* **488**, 112234 (2023).
- [47] O. Shtanko and R. Movassagh, Unitary subharmonic response and floquet majorana modes, *Physical Review Letters* **125**, 086804 (2020).
- [48] D. J. Yates and A. Mitra, Strong and almost strong modes of floquet spin chains in krylov subspaces, *Physical Review B* **104**, 195121 (2021).
- [49] J. De Nardis, D. Bernard, and B. Doyon, Diffusion in generalized hydrodynamics and quasiparticle scattering, *SciPost Physics* **6**, 049 (2019).
- [50] K. Giergiel, A. Miroszewski, and K. Sacha, Time crystal platform: From quasicrystal structures in time to systems with exotic interactions, *Physical Review Letters* **120**, 140401 (2018).
- [51] S. Anisur, W. V. Liu, and S. Choudhury, Quasi-discrete time crystals in the quasiperiodically driven lipkin–meshkov–glick model, *Entropy. An International and Interdisciplinary Journal of Entropy and Information Studies* **27**, 609 (2025).
- [52] J. Axås, B. Bäuerlein, K. Avila, and G. Haller, Data-driven modeling of subharmonic forced response due to nonlinear resonance, *Scientific Reports* **14**, 25991 (2024).
- [53] D. J. Yates, A. G. Abanov, and A. Mitra, Long-lived period-doubled edge modes of interacting and disorder-free floquet spin chains, *Communications Physics* **5**, 43 (2022).
- [54] I. Georgescu, S. Ashhab, and F. Nori, Quantum simulation, *Reviews of Modern Physics* **86**, 153 (2014).
- [55] R. Blatt and C. F. Roos, Quantum simulations with trapped ions, *Nature Physics* **8**, 277 (2012).
- [56] P. Frey and S. Rachel, Realization of a discrete time crystal on 57 qubits of a quantum computer, *Science Advances* **8**, eabm7652 (2022).
- [57] Y. Lu, W. Chen, S. Zhang, K. Zhang, J. Zhang, J.-N. Zhang, and K. Kim, Implementing arbitrary ising models with a trapped-ion quantum processor, *Phys. Rev. Lett.* **134**, 050602 (2025).
- [58] T. Weaving, A. Ralli, P. J. Love, S. Succi, and P. V. Coveney, Accurately Simulating the Time Evolution of an Ising Model with Echo Verified Clifford Data Regression on a Superconducting Quantum Computer, *Quantum* **9**, 1732 (2025).
- [59] L. Pastori, T. Olsacher, C. Kokail, and P. Zoller, Characterization and verification of trotterized digital quantum simulation via hamiltonian and liouvillian learning, *PRX Quantum* **3**, 030324 (2022).
- [60] H. Zhao, M. Bukov, M. Heyl, and R. Moessner, Making trotterization adaptive and energy-self-correcting for nisq devices and beyond, *PRX Quantum* **4**, 030319 (2023).
- [61] A. Russomanno, F. Iemini, M. Dalmonte, and R. Fazio, Floquet time crystal in the lipkin-meshkov-glick model, *Physical Review B* **95**, 10.1103/physrevb.95.214307 (2017).

- [62] H. P. Ojeda Collado, G. Usaj, C. A. Balseiro, D. H. Zanette, and J. Lorenzana, Emergent parametric resonances and time-crystal phases in driven bardeen-cooper-schrieffer systems, *Physical Review Research* **3**, 10.1103/physrevresearch.3.1042023 (2021).
- [63] M. H. Muñoz Arias, K. Chinni, and P. M. Poggi, Floquet time crystals in driven spin systems with all-to-all p -body interactions, *Physical Review Research* **4**, 10.1103/physrevresearch.4.023018 (2022).
- [64] M. Rahaman, T. Mori, and A. Roy, Phase crossover induced by dynamical many-body localization in periodically driven long-range spin systems, *Phys. Rev. B* **109**, 104311 (2024).
- [65] R. Chandra and A. Roy, Discrete Time Crystal Phase of Higher Dimensional Integrable Models, *Physics Letters A* **511**, 129552 (2024).
- [66] G. Giachetti, A. Solfanelli, L. Correale, and N. Defenu, Fractal nature of high-order time crystal phases, *Physical Review B* **108**, L140102 (2023).
- [67] R. Mattes, I. Lesanovsky, and F. Carollo, Entangled time-crystal phase in an open quantum light-matter system, *Physical Review A: Atomic, Molecular, and Optical Physics* **108**, 062216 (2023).
- [68] M. A. Fischler and R. C. Bolles, Random sample consensus: A paradigm for model fitting with applications to image analysis and automated cartography, *Communications of The Acm* **24**, 381 (1981).
- [69] F. Pedregosa, G. Varoquaux, A. Gramfort, V. Michel, B. Thirion, O. Grisel, M. Blondel, P. Prettenhofer, R. Weiss, V. Dubourg, J. Vanderplas, A. Passos, D. Cournapeau, M. Brucher, M. Perrot, and E. Duchesnay, Scikit-Learn: Machine Learning in Python, *Journal of Machine Learning Research* **12**, 2825 (2011).
- [70] N. N. Bogoljubov, V. V. Tolmachev, and D. V. Širkov, A New Method in the Theory of Superconductivity, *Fortschritte der Physik* **6**, 605 (1958).
- [71] J. G. Valatin, Comments on the theory of superconductivity, *Il Nuovo Cimento* **7**, 843 (1958).
- [72] J.-X. Zhu, *Bogoliubov-de Gennes Method and Its Applications* (Springer International Publishing, 2016) ISBN: 9783319313146.
- [73] B. Sutherland and N. Andrei, Beautiful Models: 70 Years of Exactly Solved Quantum Many-Body Problems, *Physics Today* **58**, 58 (2005).
- [74] J. Q. You and F. Nori, Superconducting Circuits and Quantum Information, *Physics Today* **58**, 42 (2005).
- [75] A. F. Kockum and F. Nori, Quantum bits with josephson junctions, in *Fundamentals and Frontiers of the Josephson Effect* (Springer International Publishing, 2019) pp. 703–741, ISBN: 9783030207267.
- [76] U. Bissbort, D. Cocks, A. Negretti, Z. Idziaszek, T. Calarco, F. Schmidt-Kaler, W. Hofstetter, and R. Gerritsma, Emulating solid-state physics with a hybrid system of ultracold ions and atoms, *Physical Review Letters* **111**, 080501 (2013).
- [77] H. Ott, Single atom detection in ultracold quantum gases: A review of current progress, *Reports on Progress in Physics* **79**, 054401 (2016).
- [78] V.-D. Nguyen, Y. Perrin, S. Le Denmat, B. Canals, and N. Rougemaille, Competing interactions in artificial spin chains, *Physical Review B* **96**, 014402 (2017).
- [79] E. Östman, U. B. Arnalds, V. Kapaklis, A. Taroni, and B. Hjörvarsson, Ising-like behaviour of mesoscopic magnetic chains, *Journal of Physics: Condensed Matter* **30**, 365301 (2018).
- [80] R. P. Cowburn and M. E. Welland, Room temperature magnetic quantum cellular automata, *Science* **287**, 1466 (2000).
- [81] A. Imre, G. Csaba, L. Ji, A. Orlov, G. H. Bernstein, and W. Porod, Majority logic gate for magnetic quantum-dot cellular automata, *Science* **311**, 205 (2006).
- [82] P. Jordan and E. Wigner, Über das Paulische äquivalenzverbot, *Zeitschrift für Physik* **47**, 631 (1928).
- [83] E. Lieb, T. Schultz, and D. Mattis, Two soluble models of an antiferromagnetic chain, *Ann. Phys.* **16**, 407 (1961).
- [84] P. Pfeuty, The one-dimensional Ising model with a transverse field, *Ann. Phys.* **57**, 79 (1970).
- [85] A. M. Tselik, Jordan–Wigner transformation for spin $S = 1/2$ models in $D = 1, 2, 3$, in *Quantum Field Theory in Condensed Matter Physics* (Cambridge University Press, Cambridge, 2003) pp. 172–178, ISBN: 9780511615832.
- [86] O. Derzhko, Jordan–Wigner Fermionization and the Theory of Low-Dimensional Quantum Spin Models. Dynamic Properties, in *Condensed Matter Physics in the Prime of the 21st Century* (World Scientific, 2008) pp. 35–87.
- [87] G. B. Mbeng, A. Russomanno, and G. E. Santoro, The quantum Ising chain for beginners, *SciPost Phys. Lect. Notes*, 82 (2024).
- [88] J. K. Pachos, Kitaev’s honeycomb lattice model, in *Introduction to Topological Quantum Computation* (Cambridge University Press, Cambridge, 2012) pp. 102–128, ISBN: 9780511792908.
- [89] M. Hermanns, I. Kimchi, and J. Knolle, Physics of the kitaev model: Fractionalization, dynamic correlations, and material connections, *Annual Review of Condensed Matter Physics* **9**, 17 (2018).
- [90] H. Takagi, T. Takayama, G. Jackeli, G. Khaliullin, and S. E. Nagler, Concept and realization of kitaev quantum spin liquids, *Nature Reviews Physics* **1**, 264 (2019).
- [91] Y. Niu, S. B. Chung, C.-H. Hsu, I. Mandal, S. Raghu, and S. Chakravarty, Majorana zero modes in a quantum Ising chain with longer-ranged interactions, *Physical Review B* **85**, 035110 (2012).
- [92] S. Sarkar, Quantization of geometric phase with integer and fractional topological characterization in a quantum ising chain with long-range interaction, *Scientific Reports* **8**, 5864 (2018).
- [93] R. R. Kumar, Y. R. Kartik, S. Rahul, and S. Sarkar, Multi-critical topological transition at quantum criticality, *Scientific Reports* **11**, 1004 (2021).
- [94] S. Rahav, I. Gilary, and S. Fishman, Effective Hamiltonians for periodically driven systems, *Physical Review A: Atomic, Molecular, and Optical Physics* **68**, 013820 (2003).
- [95] M. Bukov, L. D’Alessio, and A. Polkovnikov, Universal high-frequency behavior of periodically driven systems: From dynamical stabilization to floquet engineering, *Advances in Physics* **64**, 139 (2015).
- [96] M. Cerezo, A. Arrasmith, R. Babbush, S. C. Benjamin, S. Endo, K. Fujii, J. R. McClean, K. Mitarai, X. Yuan, L. Cincio, and P. J. Coles, Variational quantum algorithms, *Nature Reviews Physics* **3**, 625–644 (2021).
- [97] P. Virtanen, R. Gommers, T. E. Oliphant, M. Haberland, T. Reddy, D. Cournapeau, E. Burovski, P. Peterson, W. Weckesser, J. Bright, S. J. van der Walt, M. Brett, J. Wilson, K. J. Millman, N. Mayorov, A. R. J. Nelson, E. Jones, R. Kern, E. Larson, C. J. Carey, Í. Polat, Y. Feng, E. W. Moore, J. VanderPlas, D. Laxalde, J. Perktold, R. Cimrman, I. Henriksen, E. A. Quintero, C. R. Harris, A. M. Archibald, A. H. Ribeiro, F. Pedregosa, P. van Mulbregt, and SciPy 1.0 Contributors, SciPy 1.0: Fundamental algorithms for scientific computing in python, *Nature Methods* **17**, 261 (2020).

- [98] P. A. Brodtkorb and J. D’Errico, Numdifftools, <https://github.com/pbrod/numdifftools> (2022).
- [99] A. Roy, R. Dasgupta, S. Modak, A. Das, and K. Sengupta, Periodic dynamics of fermionic superfluids in the bcs regime, *Journal of Physics: Condensed Matter* **25**, 205703 (2013).
- [100] N. Lambert, E. Giguère, P. Menczel, B. Li, P. Hopf, G. Suárez, M. Gali, J. Lishman, R. Gadhvi, R. Agarwal, A. Galicia, N. Shammah, P. Nation, J. R. Johansson, S. Ahmed, S. Cross, A. Pitchford, and F. Nori, Qutip 5: The Quantum Toolbox in Python (2024), arXiv:2412.04705 [quant-ph].
- [101] C. N. Yang, Concept of off-diagonal long-range order and the quantum phases of liquid he and of superconductors, *Rev. Mod. Phys.* **34**, 694 (1962).
- [102] O. Penrose and L. Onsager, Bose-einstein condensation and liquid helium, *Phys. Rev.* **104**, 576 (1956).
- [103] J. Lajzerowicz and P. Pfeuty, Space-time-dependent spin correlation of the one-dimensional Ising model with a transverse field, *Phys. Rev. B* **11**, 4560 (1975).
- [104] S. Sachdev, *Quantum Phase Transitions*, 2nd ed. (Cambridge University Press, 2011).
- [105] D. A. Abanin, W. De Roeck, and F. çois Huvneers, Exponentially slow heating in periodically driven many-body systems, *Physical Review Letters* **115**, 256803 (2015).
- [106] R. Okuta, Y. Unno, D. Nishino, S. Hido, and C. Loomis, CuPy: A NumPy-Compatible Library for NVIDIA GPU Calculations, in *LearningSys Workshop, NeurIPS (2017) proceedings of Workshop on Machine Learning Systems (LearningSys) in the Thirty-First Annual Conference on Neural Information Processing Systems (NIPS)*. http://learningsys.org/nips17/assets/papers/paper_16.pdf.
- [107] M. Newville, R. Otten, A. Nelson, T. Stensitzki, A. Ingarciola, D. Allan, A. Fox, F. Carter, and M. Rawlik, LMFIT: Non-Linear Least-Squares Minimization and Curve-Fitting for Python (2025).